Article

Scale-up of Physics-based Models for Predicting Degradation of Large Lithium Ion Batteries

Hong-Keun Kim[1], Kyu-Jin Lee[2*]

[1] Department of Mechanical & Aerospace Engineering, Seoul National University, Seoul, 151-744, Republic of Korea ; kimhk467@gmail.com

[2] Department of Mechanical Engineering, Myongji University, Yongin, 448-728, Republic of Korea ; kjlee@mju.ac.kr

* Correspondence: kjlee@mju.ac.kr

Abstract: Large lithium-ion batteries (LIBs) in electric vehicles demonstrate different performance and lifetime compared to small LIB cells, owing to the size effects generated by the electrical configuration and property imbalance. However, the calculation time for performing life predictions with three-dimensional (3D) cell models is undesirably long. In this paper, a lumped cell model with equivalent resistances (LER cell model) is proposed as a reduced order model of the 3D cell model, which enables accurate and fast life predictions of large LIBs. The developed LER cell model is validated via the comparisons with results of the 3D cell models by simulating a 20-Ah commercial pouch cell (NCM/graphite) and the experimental values. In addition, the LER cell models are applied to different cell types and sizes, such as a 20-Ah cylindrical cell and a 60-Ah pouch cell.

Keyword: Large sized lithium-ion battery; physic-based model; life prediction; scale-up model; reduced order cell model

1. Introduction

LIBs are currently used in various systems, owing to their high energy and power density. Systems that use LIBs, such as hybrid electric vehicles (HEVs), electric vehicles (EVs), and energy storage systems (ESS), require high performance and long lifespans (over 10 years); hence, optimal design is becoming increasingly important in the development of LIBs. Although using experimental methods for fabricating and evaluating LIB cells is essential in battery design, it is difficult to fabricate cells of different sizes and shapes for optimal design. In particular, there are many limitations in time and cost while performing lifespan optimization, which requires operating and measuring batteries for long periods of time. Therefore, an approach to designing batteries along with numerical models that allow the prediction of their performance and lifespan is strongly demanded.

There are two types of LIBs models, empirical and physics-based models. Empirical models calculate the behavior of batteries with mathematical expressions based on their experimental data. A typical example of empirical models is the equivalent circuit model (ECM) [1-3], which expresses batteries as simple electrical circuits consisting of resistors and capacitors. Moreover, fitting function models [4, 5], which express the experimental results of batteries in a single equation using polynomial and power functions, are also used. As these models are simple and enable fast calculation, they are widely used in algorithms that control battery management systems (BMS) in real time. However, because these models are developed based on data obtained from specific operating conditions of the target batteries, their accuracy abruptly decreases while performing calculations on other operating conditions or if the battery is replaced. In addition, it is difficult to provide insights into electrochemical or life-reduction phenomena occurring inside the battery. In contrast, physics-based models, also known as first-principle-based models, calculate electrical, chemical, and electrochemical phenomena occurring inside the battery to predict its performance and lifespan. A typical physics-based model is the pseudo two-dimensional (P2D) model [6, 7], also called the Newman model. This model includes governing equations of several complex partial differential equations, such as ion transport and

electron conservation in porous electrodes. This model has been widely used because it accurately predicts the battery performance by considering the material characteristics and the electrode design. However, since P2D models do not consider the non-uniformity of cell volumes, they are not accurate in predicting the behavior of large-size batteries that have been recently used.

To overcome these limitations, several studies on multi-dimensional physics-based models that are able to include the actual cell shape in the calculation were proposed. Kwon [8] and Kim [9] drew fitting parameters from the experimental data of large cells and used them to propose a 2D model that allows the analysis of electric potential fields, current density distribution, and temperature distribution of pouch cells. Kim et al. [10] set independent model domains for length scales and developed a multi-scale multi-dimensional (MSMD) model framework that calculates the impact of the cell shapes considered in a higher hierarchical model domain and the electrochemical reactions calculated in a lower hierarchical model domain in a coupled manner. This enabled first-principle-based calculations on large cells. Lee et al.[11] used an MSMD model framework to develop a three-dimensional cylindrical cell model. However, the number of calculation nodes of the highest hierarchy of the structure in MSMD model frameworks is large when the model analyzes the shapes of large cells with a full resolution, resulting in long calculation times. Thus, the analysis of cell lifespans, which requires long-time operating simulations, is challenging due to long computing times.

To improve the calculation speed of physics-based models, reduced order models (ROMs) that can decrease or simplify the PDEs of governing equations have been proposed. The state-variable model proposed by Smith et al. [12] was able to improve the calculation speed by transferring full-order physics-based models into frequency domains using analytical transfer functions and numerical transfer matrices. Cai et al. [13] proposed a simplified battery model having a reduced number of PDEs using a proper orthogonal decomposition method. Guo [14] proposed a ROM that simplifies full physics-based P2D models and applied it to the analysis of 3D cells. However, as most ROMs proposed so far focused on simplifying the governing equations of electrode scales, it appears they still have computational limits when applied to cell models used to analyze large batteries.

This study proposes a LER cell model that enables fast calculations while considering the prediction of the behavior of large LIBs regarding the shape of the cell. The LER cell model corresponds to a cell domain model in the MSMD model framework. It is a simplified model that includes the electrical and thermal resistances of the cell volume of large LIB cells. The LER cell model allows for robust voltage, current, temperature response, and lifespan calculations of large cells while efficiently decreasing the grid resolution of the cell domain. In this study, the model results of the LER cell model were verified by comparing results obtained using a full-resolution 3D cell model and the experimental values of actual LIB cells. Moreover, different lifespans of various cell shapes (20-Ah pouch cell, 20-Ah cylindrical cell, and 60-Ah pouch cell) were investigated using the LER cell model.

2. Selection of domain models

As shown in Figure 1, MSMD model frameworks are structures that distinguish physical phenomena occurring inside batteries depending on lengths of scales and assign them to independent model domains. Depending on the purpose, models used in each domain can be selected and modified independently from other domains. In this study, the model domains are classified into particle (PD), electrode (ED), and cell domains (CD). Each domain model has an independent geometry and coordinate system, and data calculated in each domain are shared with the upper and lower domains inside a hierarchical structure. Owing to this hierarchical structure, in MSMD models, the number of nodes of the upper domains has a larger impact on the entire calculation time than the number of nodes of the lower domains.

In this study, the same sub-models to the particle and electrode domains are applied for investigation of the impacts of the model selected in the cell domain. In the PD model, the electrochemical and parasitic reactions occurring on the particle surface are solved by assuming a 1D spherical electrode particle, and the diffusion of lithium ions inside the particles is also calculated by Fick's law. The term "parasitic reaction" refers to electrolyte decomposition occurring on the surface of
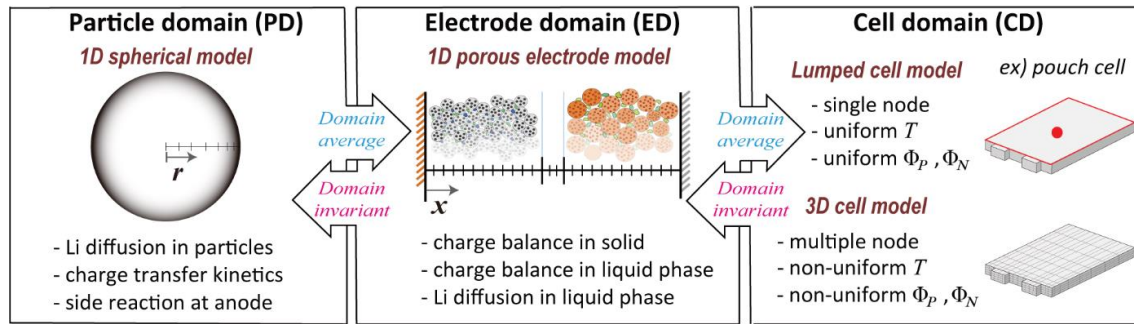
Figure 1. Concept of the MSMD model framework.

anode electrode particles, and it is used to calculate the growth of solid electrolyte interphase (SEI) layers caused by electrolyte decomposition [15-18]. In the ED model, 1D porous electrode layers are assumed to calculate the charge and lithium-ion transports that occur inside homogeneous porous electrodes. The governing equations of the particle and electrode domains are listed in Table 1. The detail information of the equations can be found in Refs. [19, 20].

2.1 Cell domain models

There are various CD models developed that consider different characteristics of various cell designs. The simplest and fastest CD model is the lumped cell model, which has just one calculation node in the CD domain. The lumped cell model assumes that the entire cell volume has a uniform electrical potential and temperature without considering the cell's shape or design in the cell domain. Thus, accurate analysis of large LIB cells may not be obtained from this model. The cell temperature in the lumped cell model is calculated using the following energy conservation equation, considering the entire cell volume as one calculation node, ignoring the heat transfer inside the cell, and considering only external heat transfer conditions. Energy conservation for lumped cell model:

$$\frac{\partial(\rho C_P T)}{\partial t} = q_{ED}^{"} - hA_s(T - T_{amb}) \tag{7}$$

$$q_{ED}^{"} = (q_{rxn,ED}^{"} + q_{joule,ED}^{"} + q_{rev,ED}^{"}) \tag{8}$$

where ρ is the density of the electrode pair, C_P is the specific heat capacity, h is the convective heat transfer coefficient, A_s is the cooling area of the cell, and T_{amb} is the ambient temperature. The volumetric heat generation in the electrode domain $q_{ED}^{"}$ is composed of electrochemical reaction heat ($q_{rxn,ED}^{"}$), joule heat ($q_{joule,ED}^{"}$), and reversible heat ($q_{rev,ED}^{"}$) [21].

CD models resolving 3D shapes of LIB cells with numbers of computational nodes are called 3D cell models in this paper. Selecting a CD model depends on the structure of composite layers composed

of electrode-separator-current collectors in the cell. When modeling pouch-type cells, a single-potential-pair-continuum (SPPC) model [10, 19] can be used as an appropriate 3D cell model for stacked composite layers that are connected in parallel in electrical tabs. Since the layer-by-layer difference is very small in the stacked composite layers of the pouch-type LIB cells, the finite volume of the cell composites can be assumed to be statistically homogeneous in the SPPC model. In one calculation node of the SPPC model, the temperature and the positive and negative electrical potential values of a pair of current collectors are calculated. For heat transfer calculations, the thermal and electrical conductivities are assumed to be orthogonal considering the layer direction of the cell volume.

To perform modeling by considering the design of cylindrical batteries, a wound potential-pair continuum (WPPC) model [11, 20], which appropriately reflects the structure of long wound composite layers, is required. In wound composite layers of cylindrical cells with a local tab, the current flows quite a long distance in the azimuthal direction along the current collectors. Owing to the electrical overpotential generated by the azimuthal current, the current collectors of adjacent composite layers have significantly different electrical potentials. Therefore, the WPPC model cannot consider an arbitrary finite volume of the electrode composite layers in the cylindrical cells as homogeneous continuum like the SPPC model. Grid mesh of the WPPC model is restricted to the wound geometry in which one calculation node includes only a pair of current collectors, thus requiring a higher number of calculation nodes when compared to SPPC models. More detailed information about SPPC and WPPC models is given in Refs. [10] and [11].

In 3D cell models such as SPPC and WPPC, the electrical potential (Φ_+, Φ_-) distribution in the metal collector plate and the temperature (T) distribution in the cell volume are calculated using the following governing equations. Potential distribution in current collectors in cell domain (CD):

$$\nabla_{CD}\left(\sigma_-^{\text{eff}}\nabla_{CD}\Phi_-\right) - j_{CD}^{'''} = 0 \tag{9}$$

$$\nabla_{CD}\left(\sigma_+^{\text{eff}}\nabla_{CD}\Phi_+\right) + j_{CD}^{'''} = 0 \tag{10}$$

Table 1. Solution variables and governing equations of the sub-domain models

	Governing equations	Boundary Conditions
1D spherical particle model		
Li$^+$ conservation in active material	$\frac{\partial c_s}{\partial t} = \frac{D_s}{r^2}\frac{\partial}{\partial r}\left(r^2\frac{\partial c_s}{\partial r}\right)$ (1)	$\left.\frac{\partial c_s}{\partial r}\right|_{r=0} = 0$, $\left.\frac{\partial c_s}{\partial r}\right|_{r=R_s} = -\frac{i^{''}}{D_s F}$
Charge transfer Kinetic (B.V equation)	$i^{''} = i_r^{''} + i_{\text{para}}^{''}$ (2) where $i_r^{''} = Fk_i(c_e)^{\alpha_a}\left(c_{s,\max} - c_{s,e}\right)^{\alpha_a}\left(c_{s,e}\right)^{\alpha_a}\left\{\exp\left[\frac{\alpha_a F}{RT}\eta\right] - \exp\left[\frac{\alpha_c F}{RT}\eta\right]\right\}$, $\eta = \phi_s - \phi_e - U_{OCV} - i^{''}R_{SEI}$ (negative electrode) , and $\eta = \phi_s - \phi_e - U_{OCV}$ (positive electrode)	
Aging mechanism (SEI layer growth)	$i_{\text{para}}^{''} = -i_{\text{para,init}}^{''}\exp\left[-\frac{\alpha_c F}{RT}\eta_{\text{para}}\right]$, $\left(i_{\text{para,init}}^{''} = Fk_{0,SEI}c_{EC}^s\right)$ (3) where $\eta_{\text{para}} = \eta = \phi_s - \phi_e - U_{\text{para}} - i^{''}R_{SEI}$, $-D_{EC}\frac{(c_{EC}^s - c_{EC}^0)}{\delta_{SEI}} = -\frac{i_{\text{para}}^{''}}{F}$, $\frac{\partial\delta_{SEI}}{\partial t} = \frac{i_{\text{para}}^{''}M_{SEI}}{\rho_{SEI}F}$, and $R_{SEI} = \frac{\delta_{SEI}}{\kappa_{SEI}}$	
1D porous electrode model		
Li conservation in liquid phase	$\frac{\partial(\varepsilon_e c_e)}{\partial t} = \frac{\partial}{\partial x}\left(D_e^{eff}\frac{\partial}{\partial x}c_e\right) + \frac{(1-t_+^0)}{F}a_s i_r^{''} - \frac{i_e^{''}}{F}\frac{\partial t_+^0}{\partial x}$ (4)	$\left.\frac{\partial c_e}{\partial x}\right|_{x=0} = 0$, $\left.\frac{\partial c_e}{\partial x}\right|_{x=L_a+L_s+L_c} = 0$
Charge conservation in liquid phase	$\frac{\partial}{\partial x}\left(\kappa^{eff}\frac{\partial}{\partial x}\phi_e\right) + \frac{\partial}{\partial x}\left(\kappa_D^{eff}\frac{\partial}{\partial x}\ln c_e\right) + a_s i_r^{''} = 0$ (5) where $\kappa_D^{\text{eff}} = -\frac{2\kappa^{\text{eff}}RT}{F}\left(1 + \frac{\partial\ln f_\pm}{\partial\ln c_e}\right)(1-t_+^0)$	$\left.\frac{\partial\phi_e}{\partial x}\right|_{x=0} = 0$, $\left.\frac{\partial\phi_e}{\partial x}\right|_{x=L_a+L_s+L_c} = 0$
Charge conservation in solid phase	$\frac{\partial}{\partial x}\left(\sigma^{\text{eff}}\frac{\partial}{\partial x}\phi_s\right) - a_s i_r^{''} = 0$ (6)	$\left.\frac{\partial\phi_s}{\partial x}\right|_{x=0} = \Phi_N$, $\left.\frac{\partial\phi_s}{\partial x}\right|_{x=L_a} = 0$ $\left.\frac{\partial\phi_s}{\partial x}\right|_{x=L_a+L_s} = 0$, $\left.\frac{\partial\phi_s}{\partial x}\right|_{x=L_a+L_s+L_c} = \Phi_P$

where σ_{+-}^{eff} is the effective conductivity of current collectors, and j_{CD}''' is the volumetric charge transfer current density. Temperature distribution in cell volume in cell domain (CD):

$$\frac{\partial(\rho c_P T)}{\partial t} = \nabla_{\text{CD}}\,(k\nabla_{\text{CD}}T) + q_{\text{CD}}'''\qquad(11)$$

$$q_{\text{CD}}''' = (q_{\text{ED}}''' + q_{\text{cc}}'')\qquad(12)$$

where k is the thermal conductivity, q_{CD}''' is the volumetric heat generation in the cell domain (CD), including the heat generation delivered from the electrode domain q_{ED}''' and the ohmic heat in the current collectors q_{cc}'''.

The selection of the CD model has a significant impact on the entire computational efficiency of the model. As shown in Figure 1, since each node of the CD model of the MSMD model framework calculates the electrode and particle domain models, increasing the number of calculation nodes in the cell domain increases the entire number of calculations and the highest iteration loop, thus significantly increasing the time required for calculations. Nevertheless, in the case of large LIB cells, if the performance and lifespan are considerably affected by the cell geometry, it is necessary to use full-resolution 3D cell models, such as SPPC or WPPC, in the cell domain to obtain more accurate predictions.

Table.2 Summary of model parameters in the sub-domain models.

Particle domain & Electrode domain	Negative electrode	Separator	Positive electrode
Particle radius, R_s (m)	4e-6[d]	-	4e-6[d]
Diffusivity, $D_{s,a}$, $D_{s,c}$ (m²/s)	1.5e-14[e]	-	2.0e-14[e]
Reaction rate constant k_a, k_c (m/s)	4.8e-11[e]	-	5.5e-11[e]
SEI layer molecular weight, M_{SEI} (kg/mol)	0.1 [17-20]	-	-
SEI layer density, ρ_{SEI} (kg/m³)	2100 [17-20]	-	-
Equilibrium potential of parasitic reaction, U_{para} (V)	0.4 [17, 19, 20]	-	-
SEI layer conductivity, κ_{SEI} (S/m)	3.8e-6[e]	-	-
Initial concentration of EC, C_{EC}^0 (mol/m³)	4541 [20]	-	-
Diffusivity of EC, D_{EC} (mol/m3)	2.0e-18 [20]		
Reaction rate for SEI layer, k0,SEI (m/s)	1.1e-15[e]		
Initial SEI layer resistance ($\Omega \cdot m^2$)	0.001		
Electrode thickness, L_a, L_s, L_c (m)	39e-6[d]	20e-6[d]	31e-6[d]
Electrolyte diffusion coefficient, D_e (m²/s)	-	3e-10[e]	-
Conductivity, $\sigma_{s,a}$,$\sigma_{s,c}$ (S/m)	100 [10]	-	10 [10]
Porosity , ε_i	0.397[d]	0.43[d]	0.404[d]
Volume fraction AB,$\varepsilon_{f,i}$	0.044[d]	-	0.042[d]
Volume fraction PVDF ,$\varepsilon_{p,i}$	0.007[d]	-	0.064[d]
Initial salt concentration, c_e, (mol/m³)		1200[d]	
Transport number, t_+^0		0.363 [19, 20]	
Faraday's constant, F, (C/mol)		96450	
Gas constant, R (J/mol·K)		8.314	

Cell domain	Pouch, 20Ah	Pouch, 60Ah	Cylindrical, 20Ah
Dimension (mm)	185×147×5.88[d]	278×195×8.85[d]	44(D)×110(h)[d]
Mass density of jelly roll (kg/m³)		2580[d]	
Specific heat of jelly roll (J/kg·K)		975[d]	
Electric conductivity for Cu, σ_- (S/m)		59.6×10⁶ [10, 11]	
Electric conductivity for Al, σ_+ (S/m)		37.8×10⁶ [10, 11]	
Thermal conductivity (W/m·K)	x , y direction : 27 [10] z direction: 0.8 [10]		azimuthal direction, k_r: 27 [11] transversal direction, k_t: 0.8 [11]
Convective heat transfer coefficient, h (W/m²·K)		25	
Initial temperature, T_{init} (ᵒC)		25	
Atmospheric temperature, T_{amb} (ᵒC)		25	

e: estimated, d: design parameter

2.2 Comparisons of lumped cell and 3D cell models

In this section, the impact of the selection of cell domain models on the lifespan analysis accuracy and calculation efficiency is compared and analyzed through analysis cases of pouch and cylindrical cells. An actual pouch-type LIB cell (20-Ah, NCM/graphite, TOP battery) was simulated by two models, one with a 3D cell model (SPPC model) and the other with a lumped cell model. The two models have the same electrode and particle domain models with the same parameters. Since the lumped cell model ignores the internal imbalances inside the cell volume while the 3D cell model considers them, comparisons of the model results can reveal effects of the large size and geometry of the LIB cell. Moreover, to identify how the cell design and size affect performances of LIB cells, the 3D cell and lumped cell models of a 60-Ah pouch cell and 20-Ah cylindrical cell are also simulated and compared.

Table 2 provides the detailed information of the three cells. The size of the 20-Ah pouch cell is the same as the reference cell (185 mm × 147 mm × 5.74 mm), and it has a 45-mm-wide electrical tab on one side. The size of the 60-Ah pouch cell is 278 mm × 195 mm × 8.85 mm, which is about three times the electrode area of the 20-Ah pouch cell. The 20-Ah cylindrical cell has a diameter of 44 mm, height of 110 mm, and the inner diameter is 8 mm. The electrodes and collector plates are spirally wound 85 times in the cylindrical cell. The length of the collector plate when unwound is about 6.55 mm. Moreover, ten 15-mm-wide tabs are placed on top of the cylindrical cell, and 10 on the bottom, separated by the same distance. The number of nodes of the cell domain is 3,000 for the 20-Ah pouch cell and 60-Ah pouch cell, and 15,000 for the cylindrical cell. The atmospheric temperature is set to 25 °C, and the top and bottom sides of both pouch cells, as well as the external side of the cylindrical cell, are cooled at a convective heat transfer coefficient of 20 W/m².

Figure 2 shows a comparative graph of the results of the 3D cell and lumped cell models with respect to constant current discharge conditions of the three types of cells at rates of 1 C, 3 C, and 5 C.
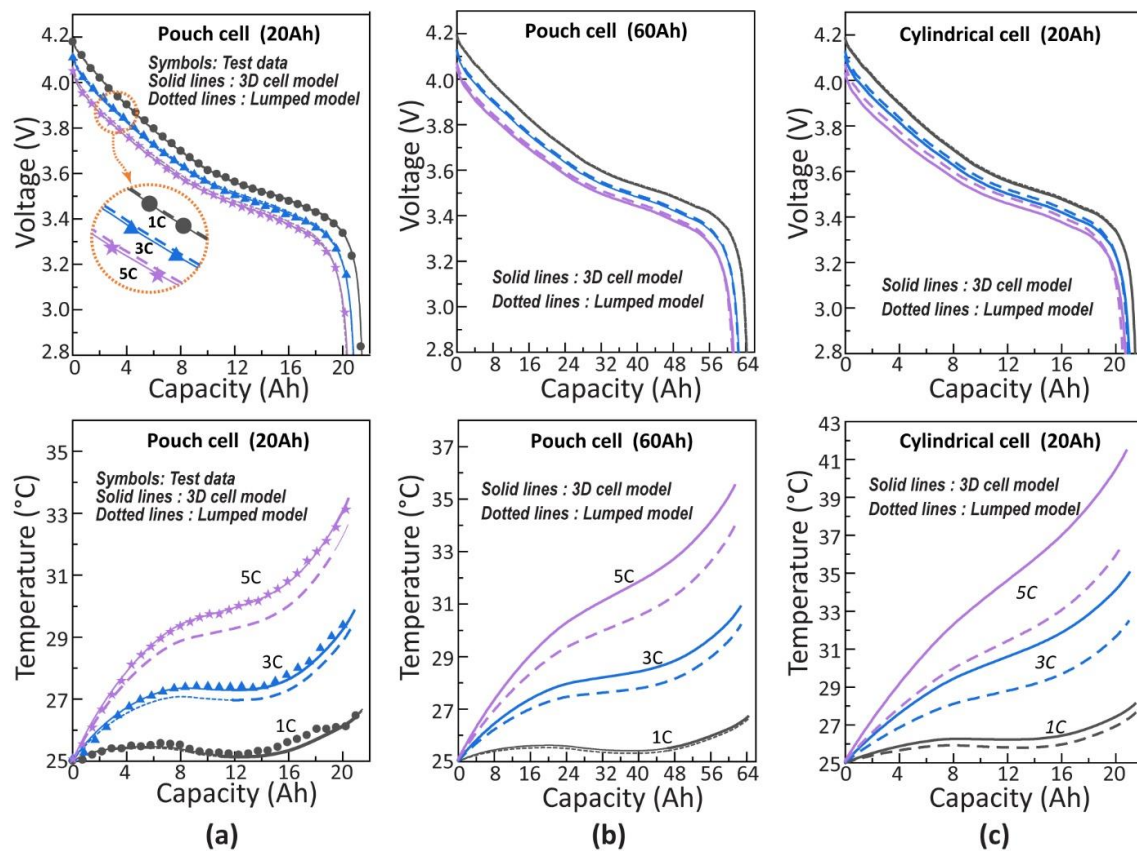

Figure 2. Comparisons of output voltages and average temperatures between the 3D cell models and the lumped models of the (a) 20-Ah pouch cell, (b) 60-Ah pouch cell and (c) 20-Ah cylindrical cell.

The experimental value of the actual 20-Ah pouch cell is also shown in Figure 2a. When looking at the output voltage shown in Figure 2a, it can be noticed that regarding the 20-Ah pouch cell, the voltage of the lumped cell model is higher (about 15 mV at 5 C), despite the small difference, than that of the 3D cell model. Moreover, the temperature of the lumped cell model is lower (about 1 °C at the end at 5 C) than that of the 3D cell model. These differences are due to the electrical overpotential and ohmic heat generation that occur in metal current collectors in the 3D cell models, which are ignored in the lumped cell models [22-24]. Therefore, as shown in Figs. 2b and 2c, these differences appear to be larger in the analysis of the 60-Ah pouch cell and cylindrical cell, which have an electrical flow path in a relatively longer collector plate than the 20-Ah pouch cell. In the cylindrical cell, whose electrical flow path reaches 65 cm, the output voltage of the 3D cell mode is lower (up to 40 mV at 5 C of discharge) than that of the lumped cell model. Likewise, when calculating the operating temperature, at 5 C of discharge, the temperature difference between the lumped cell and 3D cell models increases by a maximum of 2 °C and 6 °C, in the 60-Ah pouch cell and in the cylindrical cell, respectively. This data clarifies that, if the size of the cell increases or the electrical flow path of the collector plate is designed to be longer, the accuracy of the lumped cell model is further reduced.

However, the use of 3D cell models has certain limitations in terms of calculation time when compared to lumped cell models. Table 3 shows the number of nodes and calculation times of the lumped cell and 3D cell models. In this research, the SPPC-model-based pouch cell model uses 3,000 times more calculation nodes than the lumped cell model, and the WPPC-model-based approach uses 15,000 times more calculation nodes because the electrode's wound shape should be considered. This causes a higher number of calculation nodes required in the cell domain. Owing to this, when using one CPU, the simulation time at 1 C of discharge is 1,000 and 4,000 times longer in the SPPC cell and the WPPC cell models, respectively, when compared to the lumped cell model. Even when using eight CPUs with OPENMP parallel programming, the simulation time in the 3D cell model is about 240 (SPPC cell model) and 900 (WPPC cell model) times longer than in the lumped cell model. The use of full-resolution 3D cell models increases the iterations of the upper calculation loops, generating a significant increase in the calculation time. Thus, even when applying ROMs or ECMs, whose calculation time is shorter, to lower hierarchical models, there are still limitations in reducing the calculation time. These problems directly manifest when analyzing the lifespan of batteries.

3. Lumped cell model with equivalent resistances (LER cell model)

The impact of the cell design on the performance of large LIBs is significant, as verified in the previous section. However, high calculation costs are also required to analyze the impact of the cell design with a full-resolution cell model. To solve these problems, we propose an LER cell model that features fast calculation while considering the impact of the cell design. This LER cell model is basically a lumped cell model that calculates the positive and negative electrical potentials as well as temperature considering the cell volume as one computational node. Thus, the speed of calculation is as fast as in

Table 3. Computational costs of the LIB models.

Number of nodes		Pouch (20-Ah)	Pouch (60-Ah)	Cylindrical
	Particle domain	15	15	15
Lumped cell model	Electrode domain	25	25	25
	Cell domain	1	1	1
	Particle domain	15	15	15
3D cell model	Electrode domain	25	25	25
	Cell domain	3000	3000	15000
Calculation time (1 C discharge)		Pouch (20-Ah)	Pouch (60-Ah)	Cylindrical
Lumped cell model	1 CPU core	6.6 s	6.8 s	6.6 s
3D cell model	1 CPU core	1 h 53 min	1 h 56 min	7 h 20 min
	8 CPU core	27 min	28 min	1 h 40 min

the lumped cell model. Moreover, the LER cell model allows the prediction of the impact of the cell size and design on the performance and lifespan using the electrical and thermal resistances, which can reflect the effects of the spatial imbalance inside cell volumes. Since complex interactions among thermal, electrical and electrochemical phenomena in the cell volumes are represented by simplified resistances, it is a type of ROM that compromises analytical accuracy to ensure calculation efficiency. Building an LER cell model requires calculating the 3D cell model for determining the resistances based on the differences from the lumped cell model. A short and simple case of the 3D cell model, for example a constant current discharge in short times, is sufficient for the preparation process of the LER cell model, which can be used for long calculation, such as lifespan prediction.

The electrical resistance of the cell domain can be determined by two methods. The first is using the increase of the internal resistance in the 3D cell model compared to the lumped cell. Figure 2 shows that in all LIB cells the 3D cell model displayed a higher temperature and lower output voltage value than the lumped cell model and this tendency became more apparent with increasing C rates. The internal resistances in the 3D cell model are calculated by applying a linear polarization expression based on the model data of the three LIB cells introduced in the previous section. However, the simulations are conducted assuming that all cells were at isothermal conditions (25 °C) to remove the effects of the increased temperature in the 3D cell model. Linear polarization expressions calculate internal resistances by assuming that the discharge voltage is linearly dependent on the current density at each depth-of-discharge (DOD) as shown below [4,19]:

$$j^{''} = Y(V - U) \tag{13}$$

where Y is the electrochemical conductance ($\Omega^{-1}\text{m}^{-2}$), V is the battery's working voltage (V), U is the open-circuit voltage (V), and $j^{''}$ is the average current density (A/m^2) at the current collector. The DOD is obtained from the ratio of the discharged capacity to the cell total capacity.

In Figure 3a in the 3D cell model results of the 20-Ah pouch cell, at constant current discharge conditions (1 C– 5 C), the model data appears to be linearly dependent on the output voltage and average current density, and the slopes at all DODs, except high DODs (0.85–0.95), are similar. Each slope of the graph is the internal resistance ($R = Y^{-1}$) at each DOD condition. In the same manner as described above, the slopes at each DOD are also determined for the 60Ah pouch and 20Ah cylindrical cell. Figure 3b shows the internal resistance calculated at each DOD condition for three cells. As isothermal conditions are assumed, the lumped cell model results are the same for all cells and their internal resistance comes from electrochemical overpotential and ohmic resistance of porous electrodes, appearing in the electrode and particle domains. The highest internal resistance is calculated in the 20-
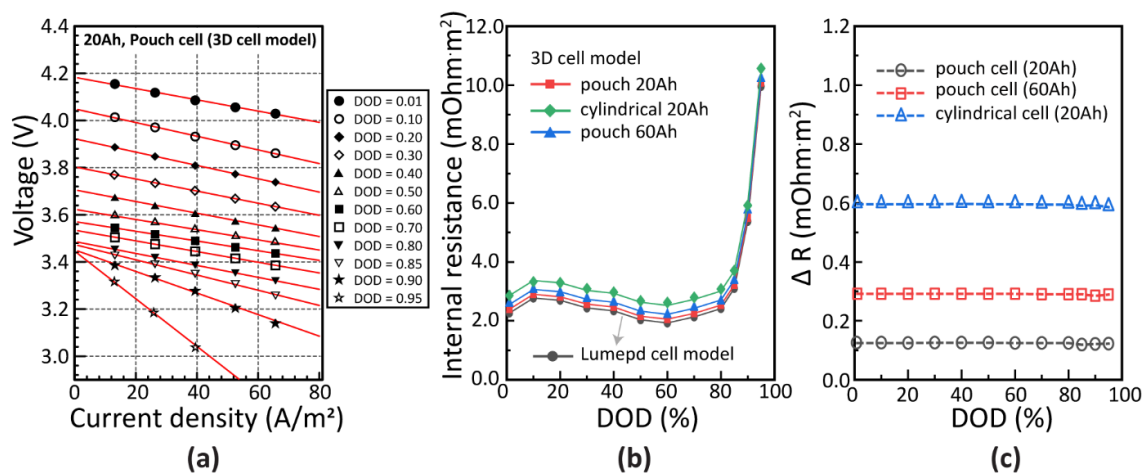

Figure 3. (a)Linear dependency of voltage and current at various DODs by 3D cell model (20-Ah pouch cell), (b) Internal resistance vs DOD for each type of cell and (c) difference of internal resistance between the lumped cell model and the 3D cell models.

Ah cylindrical cell. Figure 3c shows that the increases of the internal resistance in the 3D cell mode ΔR are 0.12, 0.29, and 0.59 mΩm^2 for the 20-Ah and 60-Ah pouch cells, and 20-Ah cylindrical cell, respectively, compared to the lumped cell model. The increases of the internal resistance in the 3D cell models are relatively constant regardless of DOD changes in Figure 3(c), while the internal resistances vary considerably from 2 mΩm^2 to 10 mΩm^2 depending on the DOD, as shown in Figure 3b. This implies that the relation between the internal resistance increments occurring in the cell domain and the electrochemical status, such as DOD, is relatively weak. Therefore, these internal resistance increments in the 3D cell model, ΔR, can be applied to the LER cell model as the electrical resistances in the cell domain, $R_{CD,E}$. The other method to determine the electrical resistance in the LER cell model is using equivalent electrical resistances of the metal current collectors. As the electrical fields in the metal collector are influenced by the plate size and the tab configuration, the analysis results of the 3D cell models are also acquired to determine the electrical resistances by this method. Figure 4 shows the electric potential distribution of the positive and negative collector plates after 5 min of starting the 1 C discharge on each cell and the equivalent electrical resistance values of the metal current collector at a 1 C discharge condition according to DOD. In Figure 4(a)-(c), during 1 C discharge, the maximum
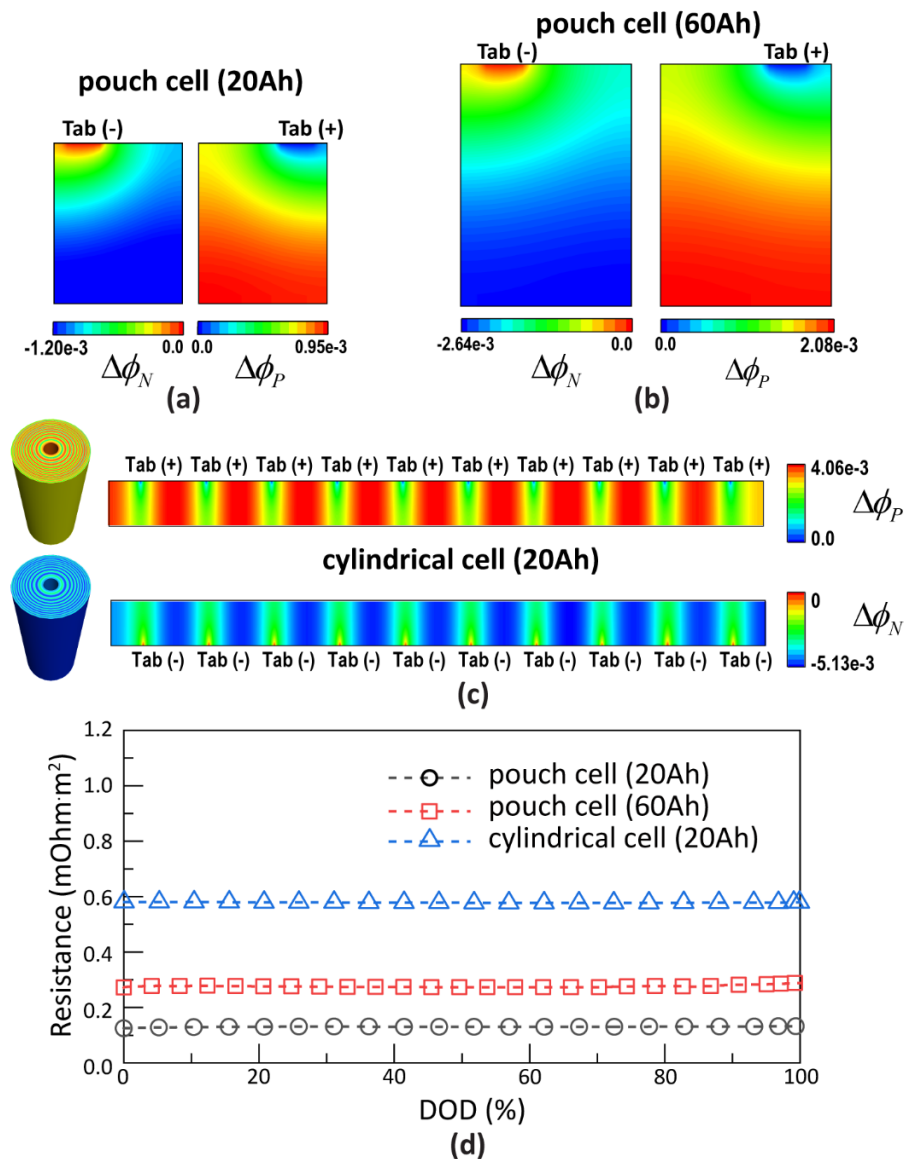

Figure 4. Contours of the electric potentials in the 3D cell models at 5 min after 1 C discharge:(a) 20-Ah pouch cell, (b) 60-Ah pouch cell and (c) 20-Ah cylindrical cell, and (d) the equivalent electrical resistance of current collectors at various DODs

electrical overpotentials inside the current collectors are 1.2, 2.6, and 5.1 mV in the 20-Ah and 60-Ah pouch cells, and in the 20-Ah cylindrical cell, respectively. To calculate the equivalent electrical resistance of the metal current collector on each cell, the average overpotential of the electric potential collector plate area is calculated with respect to the positive and negative current collectors, as shown in the equations below:

$$\Delta\overline{\Phi_P} = \frac{\Sigma\{|\Phi_P|\times v_{CD}\}}{\Sigma v_{CD}} = \frac{\Sigma\{|\Phi_P - \Phi_{P,Tab}|\times v_{CD}\}}{\Sigma v_{CD}} \tag{14}$$

$$\Delta\overline{\Phi_N} = \frac{\Sigma\{|\Phi_N|\times v_{CD}\}}{\Sigma v_{CD}} = \frac{\Sigma\{|\Phi_N - \Phi_{N,Tab}|\times v_{CD}\}}{\Sigma v_{CD}} \tag{15}$$

where Φ_P and Φ_N are the local potentials in both current collectors, $\Phi_{P,Tab}$ and $\Phi_{N,Tab}$ are tab's potentials, and v_{CD} is the finite volume in the cell domain. The equivalent electrical resistance of the current collectors R_{cc} (Ωm²) can be found using the sum of the calculated overpotentials and the average current density $\bar{J}''$ (A/m²) at the current collector.

$$R_{cc} = \frac{(\Delta\overline{\Phi_P} + \Delta\overline{\Phi_N})}{J''} \tag{16}$$

As shown in Figure 4d, the electrical resistances of the current collector obtained by Eq. (16) are relatively constant for the three types of cell regardless of the DOD and found to be 0.12, 0.29, and 0.59 mΩm² in the 20-Ah and 60-Ah pouch cells, and in the 20-Ah cylindrical cell, respectively. The calculated electrical resistance of the current collectors R_{cc} can be used as the electrical resistance in the LER cell model, $R_{CD,E}$, and almost coincides with the increase of the internal resistance in the 3D cell model, ΔR, as calculated using a linear polarization expression. This also confirms that the additional internal resistance generated by the cell design of large LIBs is mostly the electrical resistance of the collector plate, and the resistance can be represented by a constant value regardless of the DOD. Thus, in the LER cell model, the output voltage V_{LER} is calculated as follows with the output voltage V_L (V) calculated in the lumped cell model, the electrical resistance $R_{CD,E}$ and the average current density $\bar{J}''$ (A/m²):

$$V_{LER} = V_L - \bar{J}'' \, R_{CD,E} \tag{17}$$

Another scale-up effect that occurs in large LIB cells is a temperature increase caused by additional heating in the cell domain and internal heat transfer. A full-resolution 3D cell model analysis is also required to determine the thermal resistance in the LER cell model. Generally, in the case of thin pouch cells with wide surface areas, the temperature difference between the surface and the volume center is small. However, in cylindrical or large thick pouch cells, a significant temperature difference occurs between the surface and center of the cell as the thermal resistance in the through-layer direction is high. In addition, heat generated in the metal current collector is significant. Thus, in the LER cell model, the ohmic heat generation in the metal current collectors is calculated with the equivalent electrical resistance determined as $R_{CD,E}$. The equivalent thermal resistance of the cell volume is calculated based on the model results of the 3D cell model.

First, the ohmic heating generated by the electrical resistance of the metal collector is calculated through a simple Joule heating equation and summed up with heat delivered from the sub-domain models, Q_L. Thus, the total heat generation in the LER cell model, Q_{LER}, is as follows:

$$Q_{LER} = Q_L + A(\bar{J}'')^2 R_{CD,E} \tag{18}$$

where A is the total area of the electrode plate. Then, to determine the thermal resistance of the cell domain, it is assumed that a uniform heating per unit volume (q_{CD}''') occurs inside the cell, and that the cell surface is cooled at an isothermal temperature (25 °C). The steady-state temperature distribution

data inside the LIB cell, which is obtained from the model results, can be used to calculate the increase of the average temperature in the cell volume as follows:

$$\Delta\overline{T} = \frac{\sum\{(T_{CD} - T_s) \times v_{CD}\}}{\sum v_{CD}} \qquad (19)$$

This average temperature increase, $\Delta\overline{T}$, is divided by the total heat generated inside the cell, $q_{CD}'''' \cdot (\sum v_{CD})$, to determine the equivalent thermal resistance, $R_{CD,T}$, (K/W) of the cell domain.

$$R_{CD,T} = \frac{\Delta\overline{T}}{q_{CD}'''' \cdot (\sum v_{CD})} \qquad (20)$$

The calculated $R_{CD,T}$ are 5.0e-3, 3.8e-3, and 4.2e-1 for the 20-Ah and 60-Ah pouch cells, and the 20-Ah cylindrical cell, respectively. In the LER cell model, the cell temperature is calculated using the conductive thermal resistance, $R_{CD,T}$, and the convective thermal resistance $R_{conv} = hA^{-1}$, where the cooling condition is given with the convective heat transfer coefficient, h (W/m²·K) and the surface cooling area, A (m²):

$$\left(\frac{\partial \rho C_p V_{Cell} T}{\partial t}\right) = Q_{LER} - \frac{1}{(R_{CD,T} + R_{conv})}(T - T_{amb}) \qquad (21)$$

The LER cell model is established based on the procedure shown in Figure 5. First, the 3D cell model of the large LIB cell to be analyzed should be created to determine the electrical and conductive thermal resistances of the cell volume. Then, the resistances are added to a lumped cell model for calculation of the additional voltage drop, heating, and temperature increase occurring in the large LIB cell.
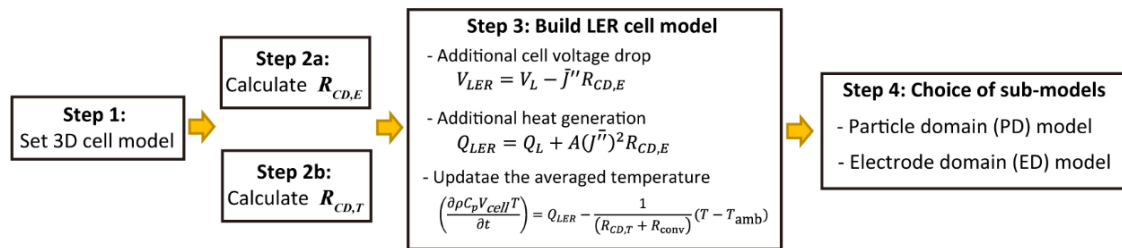

Figure 5. Procedure of the LER cell model.

4. Results and discussion

The accuracy and calculation speed were compared with the results of the 3D cell and LER cell models for the three types of cell. The cells were simulated when operating at constant current discharge conditions and under the duty-cycle conditions of ESS by the 3D cell and LER cell models. Moreover, the lifespan reduction of the cells was compared under repetitive-use conditions (4C constant current discharge, 4 C constant current charge, and constant voltage charge cycle). All simulation programs were written in the C language and calculated using a PC with 16.0 GB of RAM and an Intel Core i7-6700K 4.00-GHz CPU.

4.1. Constant current discharge simulation

Figure 6 shows graphs that compare the output voltage and average temperature calculated using the LER cell and 3D cell models under conditions in which the 20-Ah and 60-Ah pouch cells, and 20-Ah cylindrical cell discharge at a constant current from 1 C to 5 C. As the LER cell model considers the
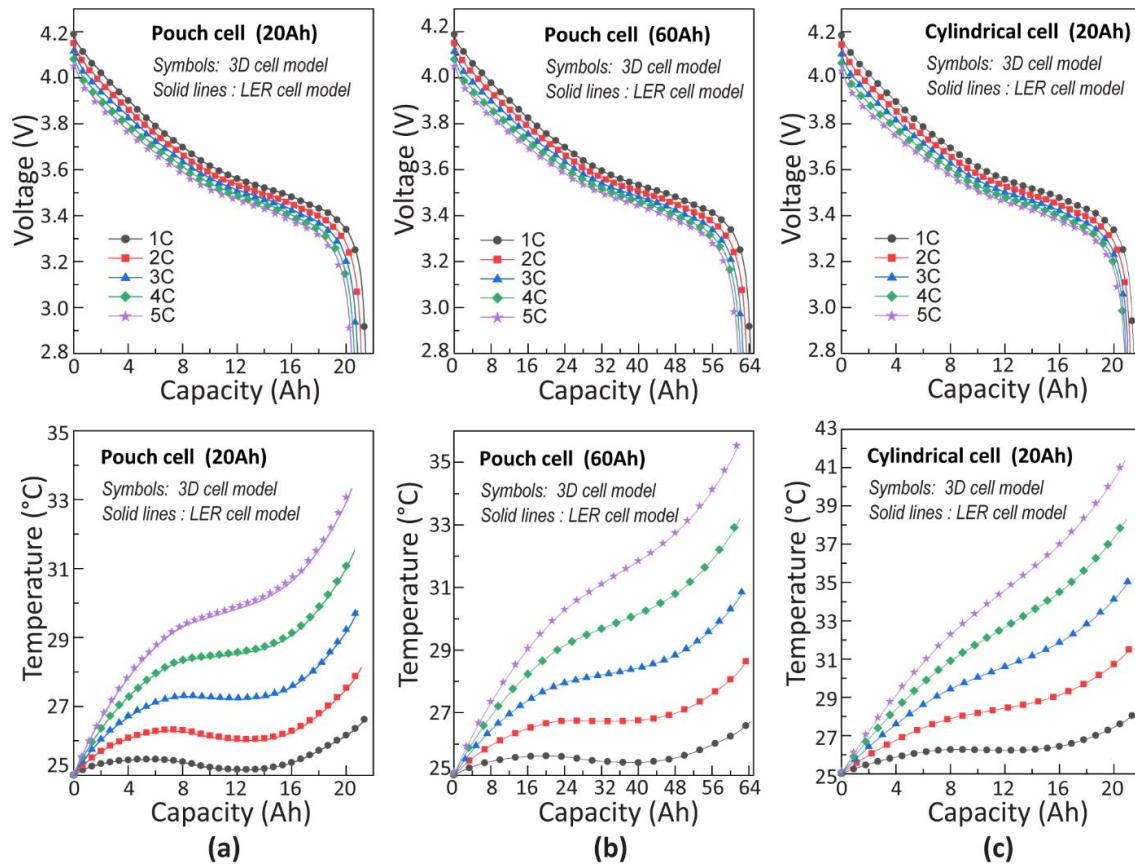
Figure 6. Output voltage and average temperature at constant current discharge conditions calculated by the LER cell and 3D cell models for (a) 20-Ah pouch cell, (b) 60Ah-pouch cell, and (c) 20-Ah cylindrical cell.

electrical resistance of the collector plate and the thermal resistance of the cell volume, the temperature increase and the output voltage drop in the large cells can be seen in the LER cell model results as in the 3D cell model results.

As shown in Figure 6, the voltage and temperature results of the LER cell model coincided with the 3D cell model results within a margin of error of 1% in the three types of cells. The difference between the LER cell and the 3D cell models comes from the simplification of the LER cell model. As the lumped mass was assumed in the LER cell model, the imbalance of electrochemical reactions inside the cell volume could not be predicted by this model. For example, as electrochemical reactions occur more actively in parts that are closer to the electrical tabs of the current collector, such parts discharge faster and become hotter. However, the effects of this imbalance were not significant because the difference between the LER cell and the 3D cell models was small.

4.2 Power profile simulation

In the response analysis of the duty cycle in which the output voltage and current of the cell shortly change, the results of the LER cell model were compared with those of the 3D cell and lumped cell models. In the power profile, the PNNL-22010 duty-cycle conditions of the ESS proposed by the Pacific Northwest National Laboratory (PNNL) were used [25]. The initial operating conditions were set to 25 °C with an initial SOC of 53.2%.
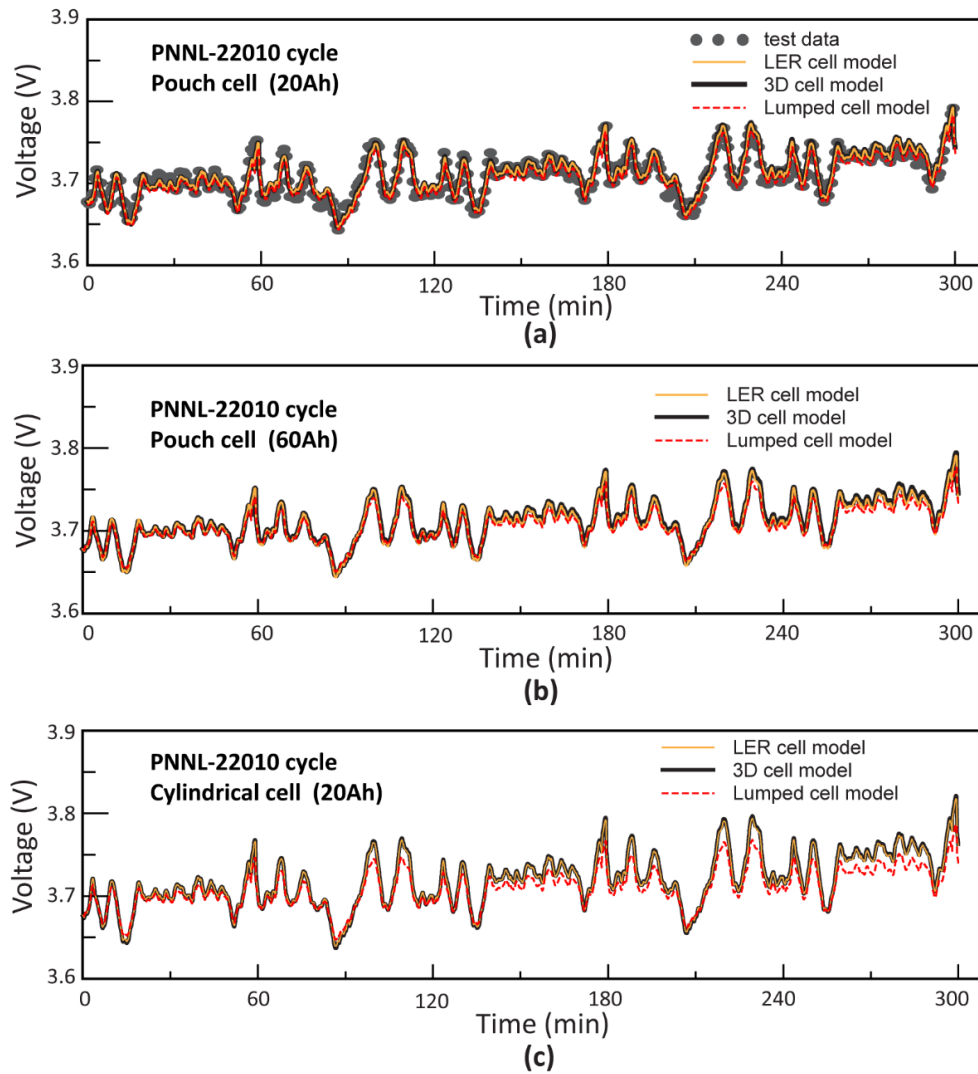
Figure 7. Output voltage at the duty cycle condition of energy storage systems calculated by the LER cell, 3D cell, and lumped cell models for (a) 20Ah pouch cell, (b) 60Ah-pouch cell, and (c) 20Ah cylindrical cell.

Figure 7 shows the voltage response results of each cell regarding a PNNL cycle of 300 min. As shown in Figure 7a, in the response of the 20-Ah cell, whose collector plate had a small resistance, the maximum voltage difference between the 3D cell and the lumped cell models was less than 3 mV, which is small. The experimental data obtained by testing the 20-Ah reference cell also met the model results. As shown in Figure 7b and 7c, in the response of the 60-Ah cell, the maximum voltage difference between the 3D cell and the lumped cell models was about 20 mV, and the highest voltage difference (45 mV) was displayed by the cylindrical cell, which had the highest collector plate resistance. With respect to all cells, the results for the LER cell model were very similar to those of the 3D cell model, which were within a margin of error of +/−1%. In the power profile cycle, the temperature increase was very low (about 1 °C) in all cells; thus, the difference between the 3D cell model and LER cell model was insignificant.

4.3 Cycle life simulation

Degradation of LIB cells is also affected by the cell size and design. The temperature increases in large cells can activate parasitic reactions, causing the lifespan of the cells to decrease more rapidly. To verify whether the LER cell model can appropriately predict this phenomenon as the 3D cell model, a cycle operation of the three cells was simulated to compare the capacity retention. The 4CD4CCCV

cycle was composed of five stages: 4 C constant current discharge (2.8 V cutoff), 30-min break, 4C constant current charge (4.2 V cutoff), 4.2 V constant voltage charge (0.05 C cutoff), and 30-min break. For all cells, the initial SOC was set to 100 %, and the initial operating and atmospheric temperatures were set to 25 °C. The 20-Ah pouch cell was cycled 2,000 times, and the experimental data and the lumped cell model results were compared. The 60-Ah pouch cell and cylindrical cell were simulated until the capacity reached 80% of their initial value.

Figure 8a shows the model results and experimentally measured values of the capacity retention of the 20-Ah pouch cell with respect to the cycle operation. The discharged capacities calculated by the LER, 3D and lumped models for 2,000 cycles displayed a margin of error of less than 1%, which meets the experimentally measured capacity. The small difference between the model results was caused by the small electrical resistance of the current collector of the 20-Ah pouch cell followed by small joule heating. Its thermal resistance was also relatively low due to its thin and wide geometry. Therefore, its temperature increase appeared insignificant to impact the degradation. In Figure 2a, it can be verified that at 5 C of discharge operation, temperature increases of the 3D cell model were within 1 °C of those of the lumped cell model. Thus, the lifespan of the 20-Ah pouch cell was not considerably affected by the cell size. Meanwhile, Figure 8b shows the capacity retention calculated for the 60-Ah pouch cell and 20-Ah cylindrical cell. In the case of the 60-Ah pouch cell, at 973 cycles, there was a difference of about 2% between discharged capacities in the LER, 3D and lumped cell model. In addition, the differences between the model results were increased up to about 6.3% at 746 cycles, for the 20-Ah cylindrical cell.
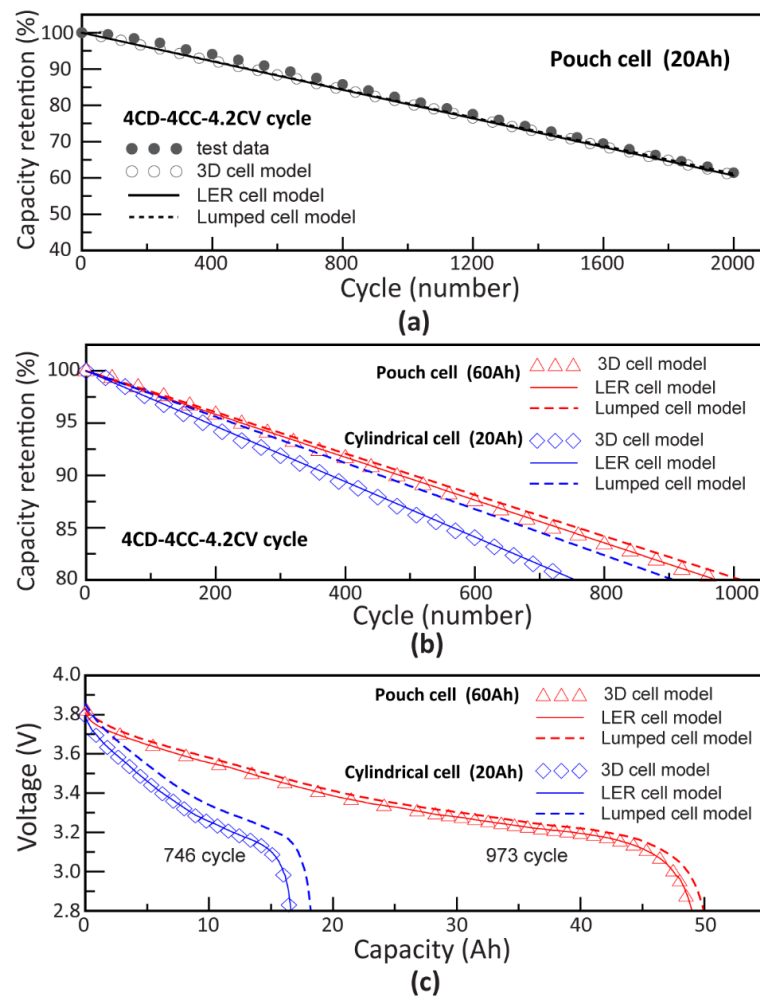

Figure 8. Comparisons of the LER cell, 3D cell, and lumped cell models: (a) capacity retention of the 20Ah pouch cell, (b) 60Ah pouch cell and 20Ah cylindrical cell, and (c) output voltages of the 60Ah pouch cell and 20-Ah cylindrical cell at 973 and 746 cycles, respectively.

It was caused by severe temperature increases in the 20-Ah cylindrical cell, considerably accelerating lifespan reduction. The discharge curves of the 60-Ah pouch cell and 20-Ah cylindrical cell, during the cycle where the discharged capacity reached 80%, are compared in Figure 8(c). Even at the end of life after a large number of cycles, the LER cell model showed almost identical voltage curves with the 3D cell model while the lumped cell model had higher output voltages (23 mV in the 60-Ah pouch cell and 110 mV in the cylindrical cell).

4.4 Comparison of calculation times

Table 4 lists the calculation times of the LER cell and 3D cell models when the simulation was conducted by a PC with 16.0 GB of RAM and an Intel Core i7-6700K 4.00-GHz CPU. Despite having conducted the 3D cell model simulation using OpenMP parallel programing with eight CPUs, the LER cell model displayed a significantly better calculation efficiency than the 3D cell model for all operating conditions. In the case of the cylindrical cell, which has a high number of computational nodes, this difference became larger; the calculation time of the LER cell model using a single CPU was down to 1/1,300 for a 4CD4CCCV cycle simulation. The 3D cell model having at least thousands of nodes in the cell domain can help to take long times for calculating the lifespan reduction through cycling simulations. It is expected that the LER cell model can be useful for predicting the lifespan of large cells accurately and effectively.

Moreover, the LER cell model in this study was developed using a full-physics model as sub-domain models that somewhat delayed the calculation time through iterative calculations. However, if the LER cell model with the equivalent electrical and thermal resistances employs the ECMs or other ROMs with fast calculations as sub-domain models, better calculation efficiency can be expected.

Table 4. Computational times of the LER and 3D cell models.

Run mode	Model	Pouch (20Ah)	Pouch (60Ah)	Cylindrical
Discharge (1CD)	3D cell model	27 min	28 min	1 h 40 min
	LER cell model	7.59 s	7.86 s	6.84 s
PNNL cycle (300 min)	3D cell model	3 day	3 day	9 day
	LER cell model	4 m 30 s	4 m 28 s	4 m 12 s
4CD4CC42CV (~80%)	3D cell model	6 day	7 day	22 day
	LER cell model	35 min	31 min	24 min

5. Conclusion

This research proposed an LER cell model that efficiently performs accurate calculations, while considering the scale-up effects that occur in large LIB cells. The developed LER cell model corresponds to the cell domain model of the MSMD model frameworks and uses the equivalent electrical resistance of the metal current collectors and the thermal resistance of the cell volume, which are factors determined by the cell design and size. Discharge test, power-profile cycle test, and lifespan reduction test results obtained from an actual commercial cell (NCM/graphite-cell-based 20-Ah pouch cell, TOP battery) were compared with the model results of the LER, 3D and lumped cell models to verify the accuracy of the LER cell model regarding the scale-effects in the large cells. In addition, model results of a virtual 60-Ah pouch cell, and a 20-Ah cylindrical cell that have the same electrode design as the test cell identified the existence of the size-effects in the large cells and how the cell design and size affect the performance and degradation. The LER cell model demonstrated calculation times as fast as the lumped cell model and displayed the same accuracy as the 3D cell model. The LER cell model is expected to be useful for analyzing the behavior or lifespan of large LIB cells in energy systems, such as electric vehicles and energy storage systems.

References

1. Klotz, D.; Schonleber, M.; Schmidt, J. P.; Ivers-Tiffee, E., New approach for the calculation of impedance spectra out of time domain data. *Electrochimica Acta* **2011,** 56, (24), 8763-8769.
2. Verbrugge, M. W.; Liu, P., Electrochemical characterization of high-power lithium ion batteries using triangular voltage and current excitation sources. *Journal of Power Sources* **2007,** 174, (1), 2-8.
3. Jung, S.; Kang, D., Multi-dimensional modeling of large-scale lithium-ion batteries. *Journal of Power Sources* **2014,** 248, 498-509.
4. Kiel, M.; Bohlen, O.; Sauer, D. U., Harmonic analysis for identification of nonlinearities in impedance spectroscopy. *Electrochimica Acta* **2008,** 53, (25), 7367-7374.
5. Sankarasubramanian, S.; Krishnamurthy, B., A capacity fade model for lithium-ion batteries including diffusion and kinetics. *Electrochimica Acta* **2012,** 70, 248-254.
6. Fuller, T. F.; Doyle, M.; Newman, J., Simulation and Optimization of the Dual Lithium Ion Insertion Cell. *Journal of the Electrochemical Society* **1994,** 141, (1), 1-10.
7. Doyle, M.; Newman, J.; Gozdz, A. S.; Schmutz, C. N.; Tarascon, J. M., Comparison of modeling predictions with experimental data from plastic lithium ion cells. *Journal of the Electrochemical Society* **1996,** 143, (6), 1890-1903.
8. Kwon, K. H.; Shin, C. B.; Kang, T. H.; Kim, C. S., A two-dimensional modeling of a lithium-polymer battery. *Journal of Power Sources* **2006,** 163, (1), 151-157.
9. Kim, U. S.; Shin, C. B.; Kim, C. S., Modeling for the scale-up of a lithium-ion polymer battery. *Journal of Power Sources* **2009,** 189, (1), 841-846.
10. Kim, G. H.; Smith, K.; Lee, K. J.; Santhanagopalan, S.; Pesaran, A., Multi-Domain Modeling of Lithium-Ion Batteries Encompassing Multi-Physics in Varied Length Scales. *Journal of the Electrochemical Society* **2011,** 158, (8), A955-A969.
11. Lee, K. J.; Smith, K.; Pesaran, A.; Kim, G. H., Three dimensional thermal-, electrical-, and electrochemical-coupled model for cylindrical wound large format lithium-ion batteries. *Journal of Power Sources* **2013,** 241, 20-32.
12. Smith, K.; Wang, C. Y., Solid-state diffusion limitations on pulse operation of a lithium ion cell for hybrid electric vehicles. *Journal of Power Sources* **2006,** 161, (1), 628-639.
13. Cai, L.; White, R. E., Reduction of Model Order Based on Proper Orthogonal Decomposition for Lithium-Ion Battery Simulations. *Journal of the Electrochemical Society* **2009,** 156, (3), A154-A161.
14. Guo, M.; White, R. E., A distributed thermal model for a Li-ion electrode plate pair. *Journal of Power Sources* **2013,** 221, 334-344.
15. Yang, X. G.; Leng, Y. J.; Zhang, G. S.; Ge, S. H.; Wang, C. Y., Modeling of lithium plating induced aging of lithium-ion batteries: Transition from linear to nonlinear aging. *Journal of Power Sources* **2017,** 360, 28-40.
16. Safari, M.; Morcrette, M.; Teyssot, A.; Delacourt, C., Multimodal Physics-Based Aging Model for Life Prediction of Li-Ion Batteries. *Journal of the Electrochemical Society* **2009,** 156, (3), A145-A153.
17. Ramadass, P.; Haran, B.; Gomadam, P. M.; White, R.; Popov, B. N., Development of first principles capacity fade model for Li-ion cells. *Journal of the Electrochemical Society* **2004,** 151, (2), A196-A203.
18. Ning, G.; White, R. E.; Popov, B. N., A generalized cycle life model of rechargeable Li-ion batteries. *Electrochimica Acta* **2006,** 51, (10), 2012-2022.
19. Kim, H. K.; Kim, C. J.; Kim, C. W.; Lee, K. J., Numerical analysis of accelerated degradation in large lithium-ion batteries. *Computers & Chemical Engineering* **2018,** 112, 82-91.
20. Kim, H. K.; Choi, J. H.; Lee, K. J., A Numerical Study of the Effects of Cell Formats on the Cycle Life of Lithium Ion Batteries. *Journal of the Electrochemical Society* **2019,** 166, (10), A1769-A1778.

21.   Viswanathan, V. V.; Choi, D.; Wang, D. H.; Xu, W.; Towne, S.; Williford, R. E.; Zhang, J. G.; Liu, J.; Yang, Z. G., Effect of entropy change of lithium intercalation in cathodes and anodes on Li-ion battery thermal management. *Journal of Power Sources* **2010,** 195, (11), 3720-3729.

22.   MeCleary, D. A. H.; Meyers, J. P.; Kim, B., Three-Dimensional Modeling of Electrochemical Performance and Heat Generation of Spirally and Prismatically Wound Lithium-Ion Batteries. *Journal of the Electrochemical Society* **2013,** 160, (11), A1931-A1943.

23.   Taheri, P.; Mansouri, A.; Yazdanpour, M.; Bahrami, M., Theoretical Analysis of Potential and Current Distributions in Planar Electrodes of Lithium-ion Batteries. *Electrochimica Acta* **2014,** 133, 197-208.

24.   Zhao, W.; Luo, G.; Wang, C. Y., Effect of tab design on large-format Li-ion cell performance. *Journal of Power Sources* **2014,** 257, 70-79.

25.   Conover, D. R.; Crawford, A. J.; Viswanathan, V.; Ferreira, S. R.; Schoenwald, D. A., Protocol for Uniformly Measuring and Expressing the Performance of Energy Storage Systems PNNL-22010 Rev. 1. In Pacific Northwest National Laboratory: Richland, Washington 2014.